



RESEARCH ARTICLE

10.1029/2018JA025507

Key Points:

- NO partial columns over altitudes 65–140 km measured at Halley, Antarctica, are on average 49% higher than SOFIE observations
- NO number density in the Antarctic mesosphere and lower thermosphere is up to $3 \times 10^8/\text{cm}^3$ higher in the 2013 winter than the 2014 winter
- Higher mesospheric NO abundance in the 2013 winter is partially explained by increased NO production due to medium-energy electrons

Correspondence to:

D. A. Newnham,
dawn@bas.ac.uk

Citation:

Newnham, D. A., Clilverd, M. A., Rodger, C. J., Hendrickx, K., Megner, L., Kavanagh, A. J., et al. (2018). Observations and modeling of increased nitric oxide in the Antarctic polar middle atmosphere associated with geomagnetic storm-driven energetic electron precipitation. *Journal of Geophysical Research: Space Physics*, 123, 6009–6025. <https://doi.org/10.1029/2018JA025507>

Received 22 MAR 2018

Accepted 4 JUL 2018

Accepted article online 20 JUL 2018

Published online 28 JUL 2018

Observations and Modeling of Increased Nitric Oxide in the Antarctic Polar Middle Atmosphere Associated With Geomagnetic Storm-Driven Energetic Electron Precipitation

D. A. Newnham¹ , M. A. Clilverd¹ , C. J. Rodger² , K. Hendrickx³ , L. Megner³ , A. J. Kavanagh¹ , A. Seppälä^{2,4} , P. T. Verronen⁵ , M. E. Andersson⁵ , D. R. Marsh⁶ , T. Kovács⁷, W. Feng^{7,8} , and J. M. C. Plane⁷

¹British Antarctic Survey, Cambridge, UK, ²Department of Physics, University of Otago, Dunedin, New Zealand, ³Department of Meteorology (MISU), Stockholm University, Stockholm, Sweden, ⁴Formerly at Finnish Meteorological Institute, Helsinki, Finland, ⁵Space and Earth Observation Centre, Finnish Meteorological Institute, Helsinki, Finland, ⁶Atmospheric Chemistry Division, National Center for Atmospheric Research, Boulder, CO, USA, ⁷School of Chemistry, University of Leeds, Leeds, UK, ⁸National Centre for Atmospheric Science, School of Earth and Environment, University of Leeds, Leeds, UK

Abstract Nitric oxide (NO) produced in the polar middle and upper atmosphere by energetic particle precipitation depletes ozone in the mesosphere and, following vertical transport in the winter polar vortex, in the stratosphere. Medium-energy electron (MEE) ionization by 30–1,000 keV electrons during geomagnetic storms may have a significant role in mesospheric NO production. However, questions remain about the relative importance of direct NO production by MEE at altitudes ~60–90 km versus indirect NO originating from auroral ionization above 90 km. We investigate potential drivers of NO variability in the southern-hemisphere mesosphere and lower thermosphere during 2013–2014. Contrasting geomagnetic activity occurred during the two austral winters, with more numerous moderate storms in the 2013 winter. Ground-based millimeter-wave observations of NO from Halley, Antarctica, are compared with measurements by the Solar Occultation For Ice Experiment (SOFIE) spaceborne spectrometer. NO partial columns over the altitude range 65–140 km from the two observational data sets show large day-to-day variability and significant disagreement, with Halley values on average 49% higher than the corresponding SOFIE data. SOFIE NO number densities, zonally averaged over geomagnetic latitudes -59° to -65° , are up to $3 \times 10^8/\text{cm}^3$ higher in the winter of 2013 compared to 2014. Comparisons with a new version of the Whole Atmosphere Community Climate Model, which includes detailed *D*-region ion chemistry (WACCM-SIC) and MEE ionization rates, show that the model underestimates NO in the winter lower mesosphere whereas thermospheric abundances are too high. This indicates the need to further improve and verify WACCM-SIC with respect to MEE ionization, thermospheric NO chemistry, and vertical transport.

1. Introduction

1.1. Background Information

Energetic particle precipitation (EPP) is an important mechanism in the polar middle and upper atmosphere, causing ionization in the neutral atmosphere and producing odd nitrogen ($\text{NO}_x = \text{NO} + \text{NO}_2$) and odd hydrogen ($\text{HO}_x = \text{OH} + \text{HO}_2$; Brasseur & Solomon, 2005; Mironova et al., 2015; Sinnhuber et al., 2012). NO_x exists mainly as NO in the thermosphere and upper mesosphere and is converted to NO_2 below 65 km (Solomon et al., 1982). Enhanced abundances of these chemical species lead to catalytic destruction of ozone (Jackman & McPeters, 2004), perturbing the radiative balance, dynamics, and large-scale circulation patterns of the atmosphere. This mechanism potentially links solar variability associated with space weather to regional surface climate (e.g., Arsenovic et al., 2016; Baumgaertner et al., 2011; Semeniuk et al., 2011; Seppälä et al., 2009, 2013).

The energetic particles, mainly protons and electrons of solar and magnetospheric origin, vary widely in energy range and the regions of the atmosphere where they impact, in both geographic/geomagnetic coverage and altitude. During solar proton events (SPE's), high fluxes of 1–500 MeV protons over the polar caps can

©2018. The Authors.

This is an open access article under the terms of the Creative Commons Attribution License, which permits use, distribution and reproduction in any medium, provided the original work is properly cited.

greatly enhance NO_x levels directly in the stratosphere leading to ozone losses exceeding 60% (Jackman et al., 2009). However, SPE's occur sporadically, most often at solar maximum and one to two years afterward, and last just a few days. At geomagnetic latitudes of 70° – 75° high fluxes of low-energy (1–30 keV) auroral electrons enter the atmosphere almost continuously and produce abundant nitric oxide (NO) in the lower thermosphere at 100–120 km, even during low geomagnetic activity (Marsh et al., 2004).

During geomagnetic storms, in the subauroral zone at geomagnetic latitudes $\leq 70^\circ$, relativistic electrons (~ 1 –4 MeV) from the radiation belts can reach the lower mesosphere and stratosphere (Horne et al., 2005). The effect of these high-energy electrons on the atmosphere is predicted to be greatest in the southern hemisphere (SH), poleward of the South Atlantic Magnetic Anomaly (SAA) region, and during the recovery phase of geomagnetic storms (Horne et al., 2009). At intermediate energies, medium-energy electron (MEE, ~ 30 –1,000 keV) precipitation will increase ionization in the polar upper stratosphere and mesosphere at altitudes ~ 60 –90 km (Turunen et al., 2009).

1.2. Previous Studies

Satellite-based observations show that MEE precipitation has a direct impact on mesospheric chemistry, with the largest hydroxyl (OH) enhancements at altitudes of 70–78 km and geomagnetic latitudes $\sim 55^\circ$ – 75° (Andersson et al., 2012; Andersson, Verronen, Rodger, Clilverd, & Wang, 2014; Verronen et al., 2011; Zawedde et al., 2016) and ozone perturbed over short timescales (Verronen et al., 2013) and in longer-term variability (Andersson, Verronen, Rodger, Clilverd, & Seppälä, 2014). The short lifetime of HO_x in the middle atmosphere restricts its effect on ozone to the mesosphere. In contrast, while the chemical lifetime of NO_x in the sunlit mesosphere and lower thermosphere is typically ~ 18 hr, in darkness NO_x can persist for months (Shimazaki, 1984; Solomon et al., 1999). This long lifetime allows auroral NO in the lower thermosphere, and mesospheric NO produced directly by MEE ionization, to be transported downward inside the polar vortex at high latitudes during winter into the stratosphere where it depletes ozone (e.g., Clilverd et al., 2007; Funke et al., 2017; Randall et al., 2007; Sinnhuber et al., 2014; Siskind et al., 2000).

In the northern hemisphere, sudden stratospheric warmings can result in the breakdown of the Arctic wintertime polar vortex and disrupt the downward transport of NO_x . However, in some of these events the stratopause and accompanying vortex reform at higher altitudes, leading to pronounced NO descent and NO_x enhancements in the middle atmosphere (e.g., Randall et al., 2009). Descent rates for the SH winter are estimated from first empirical orthogonal function mode indices of CO to be constant at 0.16–0.2 km/day below 40 km and increase almost linearly with altitude above 40 km to ~ 1 km/day at 80 km (Lee et al., 2011). However, the reliability of inferring polar winter mean air mass descent rates from remote sensing tracer gas measurements has been questioned, due to the presence of significant dynamical processes other than vertical advection (Ryan et al., 2018). Sheese et al. (2011) determined a proxy NO descent rate in the Antarctic mesosphere and lower thermosphere of 3.8 km/day, somewhat larger than mean vertical wintertime wind speeds typically presumed to be ~ 1.7 km/day. Meridional circulation reversal, which shows large wintertime variability and equatorward flow at 68°S above altitudes in the range 80–98 km (Hibbins et al., 2005; Sandford et al., 2010), could provide a barrier preventing auroral NO from descending, although diffusion will still disperse NO (Smith et al., 2011). Thus, questions remain as to whether NO produced at high altitudes (>90 km) by plentiful lower energy (1–30 keV) electrons, requiring substantial downward transport to reach the stratosphere, is more important than NO_x production in the mesosphere by medium- and high-energy (30 keV to several MeV) electrons (Clilverd et al., 2009).

Observations of NO have been made by the Solar Occultation For Ice Experiment (SOFIE) instrument (Gordley et al., 2009) on board the Aeronomy of Ice in the Mesosphere (AIM) satellite since 14 May 2007. NO volume mixing ratio and number density profiles are retrieved over the altitude range 30 to 149 km with an altitude resolution of approximately 2 km. Superposed epoch analysis of SOFIE observations over 2007–2014 by Hendrickx et al. (2015) shows a 27-day solar cycle in EPP NO production down to altitudes in the range 95–105 km and initial rapid downward transport to altitudes of 80–85 km followed by slower descent to the lower mesosphere and stratopause (~ 50 km) at a rate of approximately 1–1.2 km/day. Multiple linear regression analysis of observations from SOFIE and the Student Nitric Oxide Explorer (SNOE) showed that geomagnetic activity is the dominant source of short-term NO variability throughout the lower thermosphere at high latitudes whereas in the equatorial region solar radiation is the primary driver (Hendrickx et al., 2017).

SOFIE NO observations during a geomagnetic storm in April 2010 have been compared with model calculations incorporating a continuous 1–750 keV electron energy spectrum (Smith-Johnsen et al., 2017). This study indicates that although NO was produced directly by MEE precipitation down to 55 km, variability in mesospheric NO following the storm was mainly due to the indirect effect of downward transported NO originating from the upper mesosphere at ~75 km. Observations by the submillimeter radiometer on the Odin satellite showed increases in mesospheric NO at 75–90 km about 10 days after recurrent geomagnetic storms during the 2010 austral winter, and at all latitudes geographically poleward of 60°S, which were attributed to downward transported NO in addition to direct MEE production (Kirkwood et al., 2015).

Continuous ground-based measurements using passive millimeter-wave radiometry (Janssen, 1993) allow the temporal variations of NO and ozone within a localized region of the polar atmosphere to be studied. Observations from Antarctic stations within the SH subauroral region show large short-term enhancements of NO in the upper mesosphere and lower thermosphere (~70–105 km) related to MEE and auroral electron flux increases (Daae et al., 2012; Isono et al., 2014a, 2014b; Newnham et al., 2011, 2013). Mesospheric ozone depletions of 20–70% were observed above Antarctica during and following a moderate geomagnetic storm (minimum *Dst* of –79 nT) in late July 2009, indicating that MEE precipitation during these commonplace events may significantly affect middle mesospheric ozone distributions (Daae et al., 2012).

Major challenges remain in understanding and quantifying the contribution from MEE ionization to chemical changes in the polar atmosphere. Atmospheric simulations require accurate estimates of precipitating electron fluxes, which are difficult to determine from satellite-based measurements (Rodger et al., 2010). Also, in order to model EPP effects in the polar atmosphere below 90 km it is essential to have a detailed representation of the chemistry of the *D*-region, where cluster ions dominate and electrons are mostly attached to molecules as negative ions (Brasseur & Solomon, 2005; Sinnhuber et al., 2012; Winkler et al., 2008). Recently, new ion-neutral chemical models have been coupled into the specified dynamics (SD) version of the Whole Atmosphere Community Climate Model (WACCM 4; Marsh et al., 2013) based on the 1-D Sodankylä Ion and Neutral Chemistry (SIC) model (Verronen et al., 2005). The SIC model chemical scheme includes 70 ions, of which 41 are positive and 29 negative, and 34 neutral species with simple vertical transport (molecular and eddy diffusion). WACCM-D (Verronen et al., 2016) includes a *D*-region ion scheme of 307 reactions of 20 positive ions and 21 negative ions, allowing the 3-D global model to account for substantial HNO₃ enhancements observed in the mesosphere at altitudes ~50–80 km after major SPEs (Andersson et al., 2016). WACCM-SIC (Kovács et al., 2016) includes a more complete set of ion-neutral reactions from the detailed *D*-region ion chemistry in the SIC model, while ion-ion recombination reactions are included for three major positive ions (NO⁺, H⁺(H₂O)₃, and H⁺(H₂O)₄) and three major negative ions (O₂⁻, CO₃⁻, and NO₃⁻).

1.3. This Work

Here we study NO in the mesosphere and lower thermosphere above Antarctica during a two-year period, 2013–2014, close to the maximum of solar cycle 24. Contrasting levels of geomagnetic storm activity during the two austral winters and low levels of solar protons make this a suitable period to investigate MEE effects on the chemistry of the polar middle atmosphere. Ground-based NO measurements using passive millimeter-wave radiometry from Halley, Antarctica, are compared with satellite observations. The potential causes of significantly different levels of wintertime NO in each year are investigated using ancillary atmospheric observations and WACCM-SIC simulations, which include a representation of MEE ionization. Our results provide further evidence in support of other recent studies that identify important areas for atmospheric model development and the need for further observational data.

The manuscript is organized as follows. Section 2 outlines the geomagnetic conditions during 2013–2014 and determines occurrences of moderate geomagnetic storms. The experimental setups for Halley and satellite observations, and the atmospheric model configuration and inputs, are described in section 3. The Halley observations are presented in section 4.1 and interpreted in terms of localized NO production and transport. In section 4.2 the Halley NO partial columns are compared with SOFIE observations covering a defined geomagnetic zonal range geographically poleward of 60°S. Possible causes of significant differences between the two sets of measurements are suggested. WACCM-SIC simulation results are presented in section 4.3, and model NO number densities are compared with SOFIE data in section 4.4. Potential reasons for

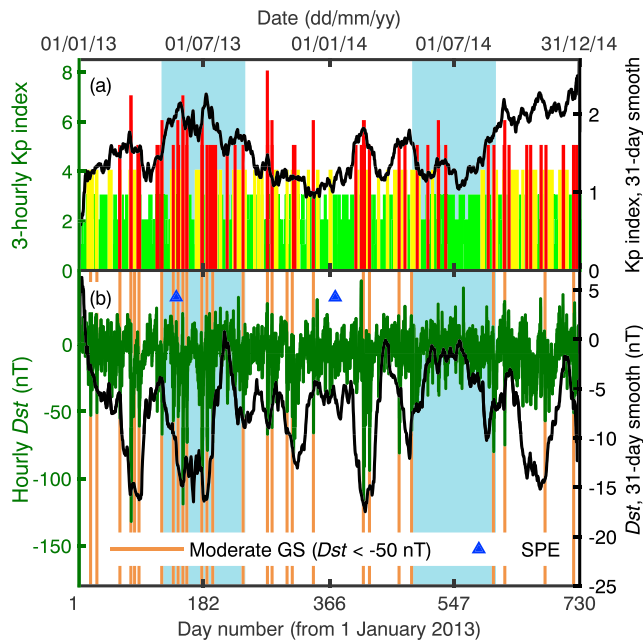


Figure 1. Time series of (a) 3-hourly Kp index and (b) hourly *Dst* index for 2013–2014. In (a) the green vertical bars are for $Kp \leq 3$, the yellow bars are $3 < Kp \leq 4$, and the red bars are $Kp > 4$. The brown vertical lines in (b) indicate the occurrences of moderate geomagnetic storms, and the blue triangles show the times of maximum proton flux for the two largest SPE's. The shaded light blue areas indicate the months May–August. Note that the 3-hourly Kp index and hourly *Dst* index, and the 31-day smoothed data, are plotted on different scales shown by the left- and right-hand axes respectively.

and geomagnetic storms occur most frequently during solar maximum and one to two years afterward. The maximum geomagnetic activity of solar cycle 24 was reached in mid-2015. No major SPE's occurred during 2013–2014. The two most significant SPE's produced only relatively modest maximum 10 MeV proton fluxes of $1,660 \text{ protons} \cdot \text{cm}^{-2} \cdot \text{sr}^{-1} \cdot \text{s}^{-1}$ on 23 May 2013 and $1,033 \text{ protons} \cdot \text{cm}^{-2} \cdot \text{sr}^{-1} \cdot \text{s}^{-1}$ on 9 January 2014 and are indicated by the blue triangles in Figure 1. Eleven smaller SPE's produced maximum 10 MeV proton fluxes in the range $14\text{--}182 \text{ protons} \cdot \text{cm}^{-2} \cdot \text{sr}^{-1} \cdot \text{s}^{-1}$ (a full list of SPE's affecting the Earth environment is available from <http://ftp.swpc.noaa.gov/pub/indices/SPE.txt>).

During 2013 and the first half of 2014 the geomagnetic storms were predominantly driven by coronal mass ejections (CMEs). CME occurrence rate tends to be highest close to solar maximum (Webb & Howard, 2012), which was in April 2014 for solar cycle 24. Contrasting geomagnetic activity during the months May–August (indicated by the blue shaded areas in Figure 1) of the two years under study is more clearly seen in the 31-day smoothed Kp indices and *Dst* data. Nine moderate geomagnetic storms occurred during the SH wintertime period in 2013 compared to only two storms in the 2014 winter, one commencing at the start of the winter period on 1 May 2014 and the other close to the end on 28 August.

3. Experimental Setup and Data Sets

3.1. Halley Observations

Observations were made from the Halley VI research station ($75^{\circ}37'S$, $26^{\circ}15'W$, L shell of $L = 4.7$, mean altitude above sea level 50 m), located on the Brunt Ice Shelf in Antarctica. As shown in Figure 2, Halley is at a geomagnetic latitude of -62° , a suitable location for observing the effects of MEE, and relativistic electron precipitation from the outer radiation belt. In wintertime Halley is also typically inside the Antarctic polar vortex, which extends from the pole to at least geographic latitude $60^{\circ}S$ and from the thermosphere down to the lower stratosphere (Harvey et al., 2004). A combination of atmospheric measurements made at Halley by

differences between the model runs and SOFIE observations are discussed in section 5 and areas suggested for future research.

2. Geomagnetic Conditions

We use disturbance storm time (*Dst*) and Kp indices to characterize geomagnetic conditions during 2013–2014. The planetary Kp index is widely used in ionospheric and magnetospheric studies as a measure of global geomagnetic activity. The Kp index quantifies disturbances in the horizontal component of Earth's magnetic field with a quasi-logarithmic integer scale in the range 0–9 where $Kp > 4$ indicates a geomagnetic storm. The *Dst* index is used to assess the strength of geomagnetic storms (Yokoyama & Kamide, 1997). During a geomagnetic storm *Dst* typically shows a sudden rise, corresponding to the storm sudden commencement, and then decreases sharply as the ring current in the magnetosphere intensifies. *Dst* zero crossings and subsequent minimum values can indicate the start and magnitude of geomagnetic storms, respectively.

The time series of the three-hourly Kp index (available from www.gfz-potsdam.de/en/kp-index) and the hourly *Dst* index (available from wdc.kugi.kyoto-u.ac.jp/dstdir) for 2013 and 2014 are shown in Figure 1. Periods of increased geomagnetic activity are shown by higher Kp index levels. During this 2-year period 28 moderate geomagnetic storms can be identified where distinct *Dst* zero crossings occur and the *Dst* index subsequently decreased to below -50 nT . The lowest *Dst* index of -132 nT occurred on 17 March 2013. The storm commencement times corresponding to *Dst* index zero crossings for each geomagnetic storm are indicated by brown vertical lines in Figure 1b. Levels of geomagnetic activity generally lag the solar cycle as defined by sunspot number and UV irradiance,

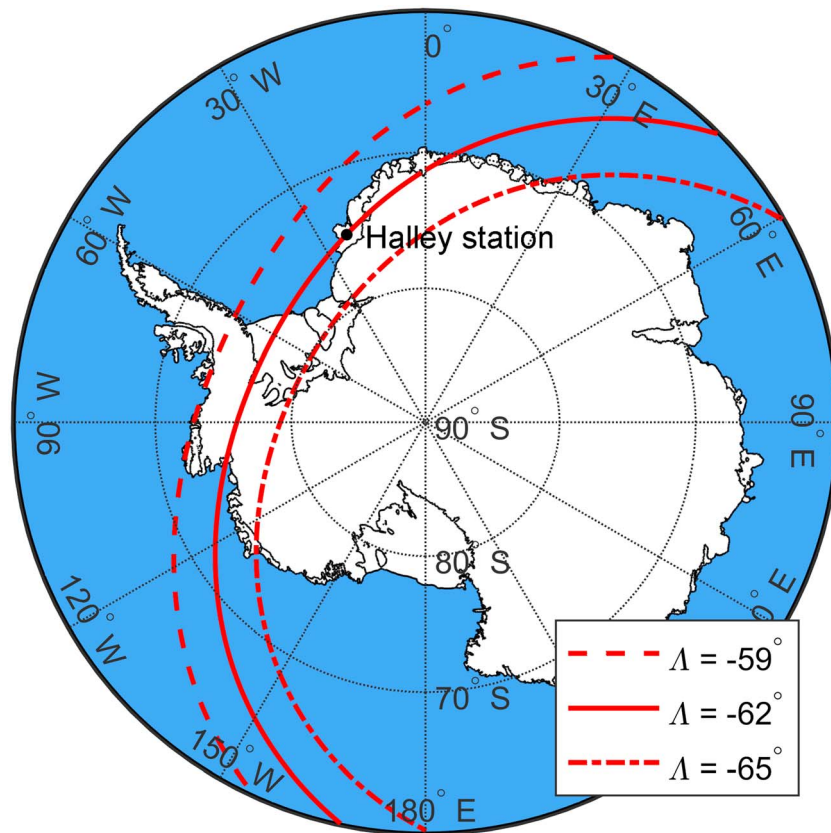


Figure 2. Map of the southern hemisphere and Antarctica poleward of geographic latitude 60°S showing the location of Halley station ($75^\circ37'\text{S}$, $26^\circ15'\text{W}$). The three red solid and dashed lines show the geomagnetic latitudes $\Lambda = -59^\circ$, $\Lambda = -62^\circ$, and $\Lambda = -65^\circ$, calculated for 1 January 2013 and an altitude of 90 km using the IGRF-12 internal field model (Thébault et al., 2015). Only the area between the dashed line ($\Lambda = -59^\circ$) and the dash-dotted line ($\Lambda = -65^\circ$) is considered in this study.

different instruments; that is, a millimeter-wave radiometer, a widebeam riometer, and a medium-frequency (MF) radar were analyzed for the study period.

Observations of temporal variations in NO abundance during the study period were provided by a ground-based millimeter-wave radiometer (Espy et al., 2006). Atmospheric observations were made at a zenith angle of 60° and azimuthal angle of 163° . Assuming negligible refraction, the radiometer view intercepted altitudes of 65–140 km at horizontal distances in the range 113–242 km approximately south of Halley. The radiometer was housed in a customized caboose maintained at a temperature of ~ 290 K with the atmospheric view through an extruded polystyrene foam vertical window. The window material provided good millimeter-wave transmission and thermal insulation properties with minimal snow deposition or degradation under extreme conditions with temperatures as low as -55°C , instantaneous wind speeds in excess of 25 m/s, and exposure to solar UV radiation. The caboose location ~ 2.5 m above the surface minimized the adverse effects of blowing snow on the millimeter-wave observations. During blowing snow conditions, which occur at Halley about 30% of the time during winter, the particle number density at heights above 1 m is more than 10 times lower than just above the surface (Mann et al., 2000) leading to reduced scattering attenuation of the millimeter-wave signal. The NO emission line centered at 250.796 GHz, down-converted to $\sim 1,350$ MHz, was measured using a chirp transform spectrometer (Hartogh & Hartmann, 1990; Villanueva et al., 2006; Villanueva & Hartogh, 2004) with 14 kHz resolution and 40 MHz bandwidth. Daily mean calibrated brightness temperature spectra were calculated from the average of 20.5 hr of NO observations each day, recorded at 00:30–06:00, 06:30–12:00, 14:00–18:00, and 18:30–23:59 UTC. NO measurements were made on 508 days between 1 March 2013 and 30 July 2014, that is, 98.3% of the total 517 days. Data gaps ranging from a few hours to approximately two days were due to electrical power loss resulting in instrument

shutdown or routine maintenance. Limited electrical power at Halley station meant that the radiometer could not be operated between 31 July and the end of 2014.

A widebeam riometer (Little & Leinbach, 1959; Rodger et al., 2012) was used to measure cosmic radio noise absorption at 30 MHz, providing an indication of energetic electron precipitation (EEP). This ground-based instrument receives signal over an angle $\pm 60^\circ$ of zenith and probes an ~ 190 - to 310-km-wide cone of the ionosphere directly above Halley station. The region of the atmosphere measured by the riometer overlaps the co-located millimeter-wave radiometer observations. Part of the energy of the cosmic radio noise propagating through the ionosphere is absorbed due to collisions of free ionospheric electrons with neutral atoms. Increased atmospheric opacity in the frequency range 15–70 MHz is caused by increased electron concentration in the *D*-region that can arise from EEP. Typically, the absorption peaks near 90 km altitude where the product of electron density and neutral collision frequency is largest. The instantaneous changes in cosmic noise absorption (ΔCNA , in dB) for each 24 hr period were calculated as the ratio of the measured signal intensity received at the ground to the quiet day curve (QDC) absorption (Krishnaswamy et al., 1985). The QDC characterizes the normal variation in CNA due to sidereal changes in the intensity of cosmic noise entering the atmosphere and background ionospheric absorptions not strongly associated with geomagnetic storms. Daily QDC curves were determined by identifying periods of low geomagnetic activity and applying sidereal time corrections to the corresponding riometer data. The daily mean riometer absorption was calculated for each 24-hr period (00:00–23:59 GMT) between 1 March 2013 (day 60) and 30 July 2014 (day 211).

Daily mean wind speeds in the mesosphere and lower thermosphere for the study period were determined from observations by a MF radar that operated quasi-continuously at Halley from February 2012 until January 2017. Five cross-dipole antennas transmitted pulses in O-mode polarization at 2.7 MHz and 100 kW peak power. The wind structure of the mesosphere was probed using measurements of the radar signal partially reflected from gradients in electron density within the *D* region. The signal scattered by the atmosphere was received by three antennas located above the snow surface and sampled by 24×2 km range gates centered on altitudes from 52 to 100 km. Horizontal wind profiles were retrieved using the full correlation analysis technique (Briggs, 1984) and averaged to provide daily mean wind speeds.

3.2. Satellite Observations

In this study we analyzed data from two satellite observing systems: National Oceanic and Atmospheric Administration (NOAA) Polar Orbiting Environment Satellites (POES) and the SOFIE. These instruments provide observations of MEE fluxes and NO vertical profiles, respectively.

Energetic electron measurements are made by the Medium Energy Proton and Electron Detector (MEPED; Evans & Greer, 2004; Hendry et al., 2017; Rodger et al., 2010), part of the Space Environment Monitor 2 (SEM-2) instrument package on board the NOAA POES, which are in high-inclination Sun-synchronous orbits at altitudes of ~ 800 – 850 km. Here we used data (available from <http://www.ngdc.noaa.gov/stp/satellite/poses/dataaccess.html>) from the MEPED 0° electron telescope, which points radially outward along the Earth-satellite direction with $\pm 15^\circ$ width and provides three channels of energetic electron data: >30 keV (0e1 channel), >100 keV (0e2 channel), and >300 keV (0e3 channel). Poleward of geomagnetic latitude 33° , the 0° electron telescope monitors electrons in the bounce loss cone that will enter the Earth's atmosphere. We apply a proton correction algorithm (available from the Virtual Radiation Belt Observatory, <http://virbo.org>) to these data as described in Lam et al. (2010, Appendix A). These corrected data were then used to determine daily mean electron count rates for the >30 keV channel, >100 keV channel, and >300 keV channel (Yando et al., 2011) between $L = 3.5$ and 5.5 . This L-shell range covers the extent of the Halley ground-based observations and is equivalent to the geomagnetic latitudes 57 – 65° and the locations of the inner and mid parts of the outer radiation belt. The daily mean count rates of the >300 keV channel were subtracted from those of the >100 keV channel to estimate the electron count rate (ECR100) for precipitating electrons in the 100–300 keV energy range that will deposit the majority of their energy into the atmosphere at altitudes of 70–80 km. Similarly, the daily mean count rates of the >100 keV channel were subtracted from those of the >30 keV channel to estimate the count rate (ECR30) of electrons in the 30–100 keV energy range that will produce strongest ionization in the atmosphere at ~ 75 – 110 km.

We used NO vertical profiles from the SOFIE (Gordley et al., 2009) on the AIM satellite. During the observation period 2013–mid-2014 SOFIE made 15 sunrise and sunset occultation measurements each day in the SH. NO

profiles are retrieved from measurements of the 5.32 μm absorption band and cover the altitude range 30–149 km with height resolution of approximately 2 km. The methods described in Hendrickx et al. (2015), and estimated uncertainties from Gómez-Ramírez et al. (2013), were used to determine daily mean zonal average NO number density profiles over the geomagnetic latitude range -59° to -65° and geographically poleward of 60°S from processed SOFIE data (version 1.3, available from sofie.gats-inc.com).

3.3. Model Simulations

For this study, atmospheric calculations were performed using WACCM-SIC as described in Kovács et al. (2016). The model was used in SD mode, nudged up to ~ 0.79 hPa toward the Modern-Era Retrospective Analysis for Research and Applications (MERRA) reanalysis of National Aeronautics and Space Administration (NASA)'s Global Modeling and Assimilation Office (Rienecker et al., 2011), and transitioning linearly above this level to a free running atmosphere. The simulations followed the reference chemistry climate model (REF-C1SD) forcing scenario from the SPARC Chemistry Climate Model Initiative (Eyring et al., 2013). Solar fluxes were from the Naval Research Laboratory (NRLSSI v.1) empirical solar model and vary daily, while the parameterized auroral forcing varied with the daily Kp index. The model was run with enhanced eddy diffusion rate (Prandtl number 2), which improves representation of trace species concentrations in the mesosphere and lower thermosphere (Garcia et al., 2014; Smith, 2012). The global model simulation data were output at 88 pressure levels from the surface to 5.96×10^{-6} hPa (~ 140 km altitude) and at a horizontal resolution of $1.9^\circ \times 2.5^\circ$ (latitude \times longitude). Daily mean NO number density profiles for 2013–2014 were calculated using WACCM-SIC data at model grid points within the geomagnetic latitude range -59° to -65° and geographically poleward of 60°S to match the selected sampling of the SOFIE observations used in this study.

Two WACCM-SIC runs were performed, a *no MEE* run using the standard parameterization for auroral electron precipitation in WACCM and a *MEE* run in which the auroral mechanism was supplemented with MEE ionization. The methodology for calculating MEE ionization rates was similar to that described in Orsolini et al. (2018). This method is based on direct satellite measurements by the MEPED instrument rather than the proxy-based parameterizations (e.g., Matthes et al., 2017; van de Kamp et al., 2016) developed as part of the long-term solar forcing data set recommended for the sixth phase of the Coupled Model Intercomparison Project (CMIP6). However, different from Orsolini et al. (2018), we changed the energy range from 50–2,000 keV to 30–1,000 keV to be consistent with the CMIP6 recommendation. We also used an improved method by Fang et al. (2010) to calculate the atmospheric ionization rates. WACCM-SIC provided the model atmosphere that was used in the ionization rate calculations.

For MEE ionization rate estimation we used electron fluxes observed by the 0° MEPED telescope. Measurements in the three electron channels >30 keV (0e1 channel), >100 keV (0e2 channel), and >300 keV (0e3 channel) with values $<250 \text{ el} \cdot \text{cm}^{-2} \cdot \text{s}^{-1} \cdot \text{sr}^{-1}$, approaching the minimum detectable flux ($\sim 100 \text{ el} \cdot \text{cm}^{-2} \cdot \text{s}^{-1} \cdot \text{sr}^{-1}$), were set to zero. Similarly, all electron observations around the SAA and when the MEPED P7 omni-directional detector reports >36 MeV protons were excluded. Electron observations from each integral channel were combined from all operational POES instruments by zonally averaging the measurements in geomagnetic coordinates with 3-hr time resolution and 0.5 L resolution over $L = 2.25$ – 9.75 , which encompasses the outer radiation belt. It has previously been shown that power laws are an accurate representation of the EEP flux spectrum, that is, through a comparison of high energy resolution DEMETER electron flux observations with POES MEPED measurements (Whittaker et al., 2013). Hence, we fitted a power law spectrum to the three 0° electron telescopes (i.e., 0e1 channel, 0e2 channel, and 0e3 channel) to obtain the energy spectral gradient (k) for the precipitating electrons.

The power law fitted EEP parameters were then used to determine ionization rates assuming that the EEP had a differential power law flux spectrum covering the energy range 30–1,000 keV using 168 logarithmically spaced bins. The ionization rate calculation was based on a continuously slowing-down approximation and a normalized energy dissipation distribution function for electrons (Rees, 1989). A prior WACCM simulation provided daily zonal mean neutral background data for the ionization rate calculation. The Fang et al. (2010) parameterization of atmospheric ionization by isotropically precipitating monoenergetic (100 eV to 1 MeV) electrons was used. Ionization rates were calculated with 3-hr time resolution for each of the L-shell bins (latitudes), after the differential electron fluxes were integrated over pitch angles 0 – 80° and azimuth angles 0 – 360° assuming an isotropic angular distribution. The L shell-dependent ionization rates were then

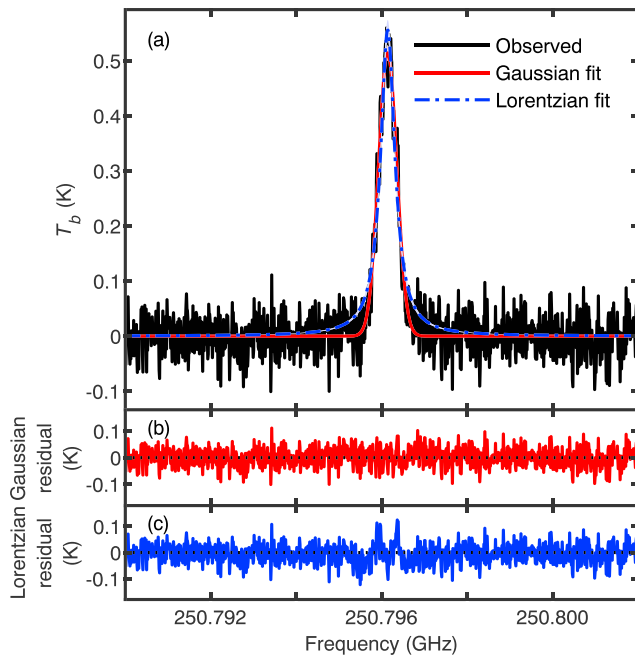


Figure 3. (a) Halley radiometer daily mean NO observation for 2 July 2013 (day 183), Gaussian and Lorentzian line-fits, (b) observed minus Gaussian line-fit residual, and (c) observed minus Lorentzian line-fit residual.

converted to geomagnetic latitude and, with the assumption of uniformity on magnetic longitude, projected onto the WACCM grid points.

4. Results

4.1. Radiometer NO Partial Columns

Figure 3a shows a 12 MHz section of the daily mean brightness temperature spectrum for 2 July 2013 (day 183), centered on the NO emission at 250.796 GHz. A smoothly varying baseline of ~ 73 K has been subtracted from the atmospheric spectrum by fitting a four-term polynomial to the data excluding the region within ± 1.5 MHz of the NO peak. The baseline contains broadband components of the atmospheric spectrum including the water vapor continuum and the wings of pressure-broadened ozone lines. The root-mean-square noise of the spectrum is 33 mK. The observed NO emission line is fitted to single Gaussian and single Lorentzian curves, with the best fit results shown in Figure 3a. The observed-minus-fit residuals (Figure 3b) for the Gaussian curve (coefficient of determination, $R^2 = 0.87$) are at the root-mean-square noise level whereas for the Lorentzian curve ($R^2 = 0.86$) the residual signal exceeds the noise level in the line wings. The full-width half-maximum of the Gaussian fit is 503(11) kHz. This indicates that thermal, Doppler-broadened NO emission from altitudes above ~ 65 km dominates the observed signal, as was found in measurements from Syowa station, Antarctica, during 2012–2013 (Isono et al., 2014a, 2014b).

Gaussian curves were fitted to all observed daily mean spectra where the maximum baseline brightness temperature was below 120 K, corresponding to atmospheric transmittance higher than 0.95. The spectrum baselines were modeled as described above by selecting either a two-, three-, or four-term polynomial or a sine curve to achieve the best fit. Daily mean NO partial column densities above ~ 65 km were determined from the integrated intensities of the NO emission line brightness temperature using the method described in Isono et al. (2014b). The upper range of the NO partial column is estimated to be 140 km since thermal-broadened emission from NO molecules above this altitude makes a negligibly small contribution to the measured integrated intensities. The integrated intensities were determined from the area under each fitted Gaussian curve, with uncertainties estimated from the 95% confidence bounds, that is, ± 2 standard deviations (σ), of each fit. Rather than assuming a constant atmospheric temperature for the column density estimation we use the mean daily temperature calculated over altitude range 65–140 km from SD-WACCM data.

Figure 4a shows the time series of observed daily mean NO partial columns for altitudes above 65 km. Large day-to-day variability in the partial columns can be attributed to short-term NO production and transport. Abrupt increases in mesospheric and lower thermospheric NO coincide with occurrences of moderate geomagnetic storms and high riometer absorption (Figure 4b), which indicates increased ionization at ~ 75 –90 km above Halley. The 31-day moving averages smooth the short-term variability of NO abundances and riometer absorption, enabling longer-term seasonal variations during 2013–2014 to be seen more clearly. During both years NO shows strong seasonal variability with substantially higher partial columns during the austral winter months May–August (indicated by the blue shaded areas). At this high latitude (76°S), during winter the middle and upper atmosphere remains in near darkness for long periods (Figure 4c). Very low levels of solar illumination are present in the atmosphere 90 km above Halley when solar elevation is $\leq -20^\circ$, which is for a maximum ~ 14 hr at winter solstice. During austral summer solar elevation is $\geq 0^\circ$ in the mesosphere during a 70-day period from 1 November to 9 February (day numbers 305 to 406). Throughout the 2013–2014 austral summer, despite increased ionization as indicated by riometer absorption, NO partial columns were low due to photolysis losses exceeding production in the mesosphere and lower thermosphere. However, high levels of NO occurred during the early part of 2013 when production associated with a series of closely spaced moderate geomagnetic storms overcomes losses in the sunlit atmosphere. The lowest Dst index (-132 nT) of 2013–2014 occurred on 17 March 2013 (day number 76) during a

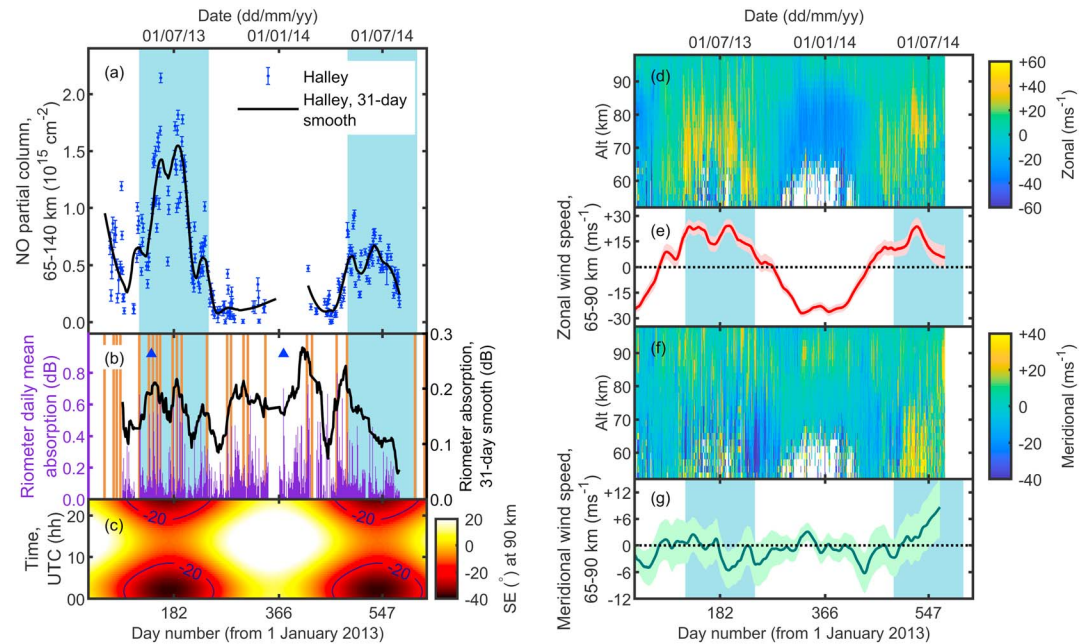


Figure 4. Overview of observations from Halley station, Antarctica in 2013–2014: (a) radiometer daily mean and 31-day smoothed NO partial column density for altitudes above ~65 km; (b) daily mean and 31-day smoothed 30 MHz wide-beam riometer absorption; (c) diurnal variation in solar elevation (SE) angle calculated for an altitude of 90 km above Halley, where time is UTC; (d) MF radar zonal winds (+ve = eastward), (e) 31-day smoothed MF radar zonal winds averaged over 65–90 km; (f) MF radar meridional winds (+ve = northward); and (g) 31-day smoothed MF radar meridional winds averaged over 65–90 km. The shaded light blue areas in (a), (b), (e), and (g) indicate the months May–August. The brown vertical lines in (b) indicate the occurrences of moderate geomagnetic storms, and the blue triangles show the times of maximum proton flux for the two largest SPE’s during 2013–2014. For the MF radar data in (e) and (g) the shaded areas are the 95% confidence intervals (± 2 standard deviations) of the 31-day smoothed winds. Note that the riometer daily mean absorption and the 31-day smoothed data in panel (b) are plotted on different scales shown by the left- and right-hand axes respectively.

CME-driven storm (Søråas et al., 2017). Higher values of NO partial column are observed during the 20 days following this event.

A particularly striking feature in the observed NO is the difference between the two winter periods. Although NO partial columns are similar during late autumn and the start of winter in both years, during the first half (May–June) of the 2013 winter the partial columns continue to increase and by mid-winter are up to $1.0 \times 10^{15}/\text{cm}^2$ higher than at the corresponding time in 2014. During 2013 the partial columns reach maximum values either side of midwinter, whereas in 2014 the highest daily mean values are at the start of winter, shortly after the geomagnetic storm on 1 May 2014. For both winters, increased NO generally coincides with the occurrences of geomagnetic storms and higher riometer absorption.

The potential roles of atmospheric transport and dynamics in adding complexity to the NO partial column variations, by redistributing NO, are indicated by the Halley MF radar wind speed data shown in Figures 4d–4g. Although the zonal and meridional winds show large day-to-day variability, distinctly different patterns of mesospheric wind speed and direction are observed for the two winters. Eastward winds typically develop during late autumn (April) at altitudes of 60–90 km above Halley and strengthen as the wintertime polar vortex becomes established. In 2013 the strong early wintertime zonal winds weakened around solstice before strengthening again in the latter part of the winter, whereas in the 2014 winter initially strong eastward winds above ~70 km decreased after solstice. The strongest eastward winds, and dips in wind speed during both winters, coincided with observed variations in NO partial column. During the 2014 winter the strongest eastward winds appeared at 70–80 km at the same time as the second peak in NO and declined in strength as the NO partial column decreased. Throughout the 2013 winter meridional winds were predominantly equatorward (i.e., northward) at altitudes above ~80 km and poleward below ~80 km. The

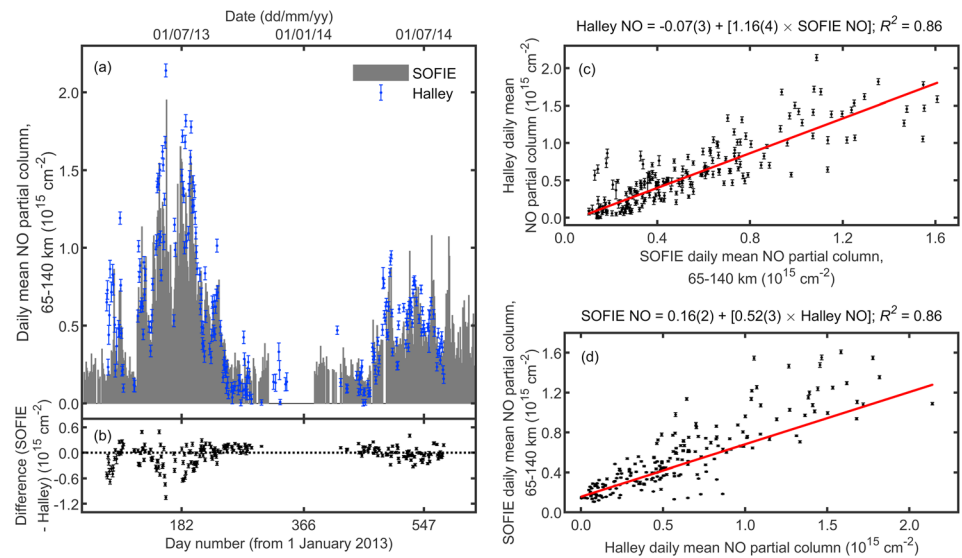


Figure 5. (a) Time series of daily mean Halley radiometer and SOFIE NO partial column density over the altitude range 65–140 km, (b) differences between the observed partial column densities, and (c and d) linear least squares regression analyses for the observed partial column densities with SOFIE and Halley data, respectively, as regressors and the red lines indicating the best fit lines. The error bars are $\pm 1\sigma$.

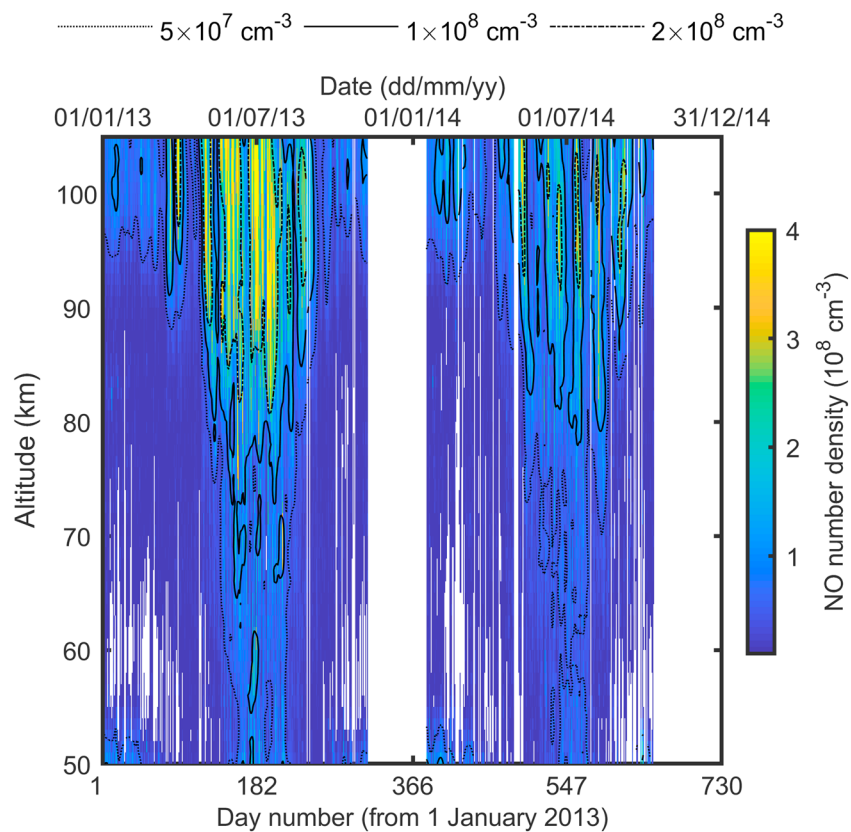


Figure 6. Time series of SOFIE daily mean NO number density during 2013–2014. The data set is for satellite observations within the geomagnetic latitude range -59° to -65° and geographically poleward of 60° S. The dotted, solid, and dot-dashed lines show isopleths at 5×10^7 /cm 3 , 1×10^8 /cm 3 , and 2×10^8 cm $^{-3}$ of the 11-day smoothed NO number density. The white panels indicate gaps in data coverage.

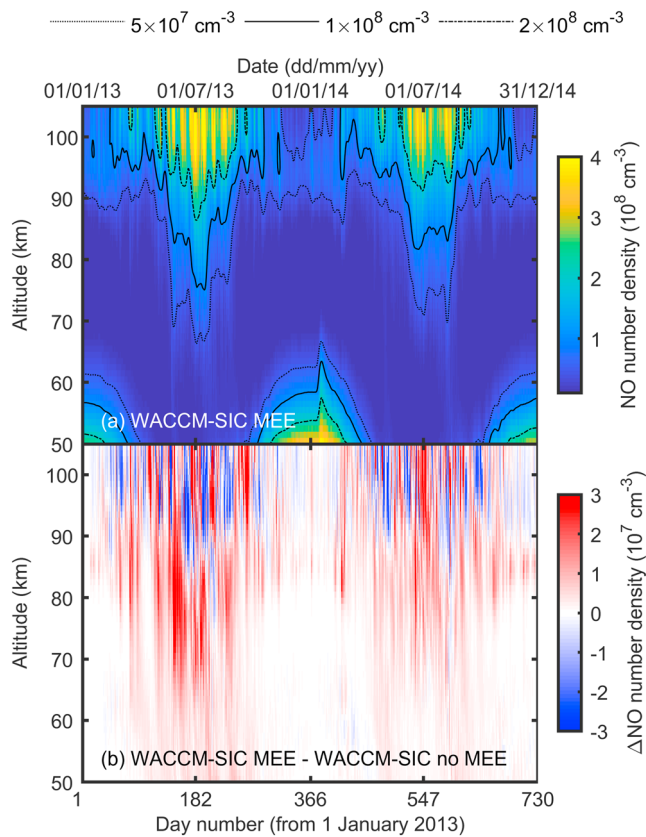


Figure 7. Time series of daily mean NO number density profiles during 2013–2014, for the geomagnetic latitude range -59° to -65° and geographically poleward of 60°S , from WACCM-SIC simulations (a) including MEE ionization and (b) differences between the two model runs. In (a) the dotted, solid, and dot-dashed lines show isopleths at $5 \times 10^7/\text{cm}^3$, $1 \times 10^8/\text{cm}^3$, and $2 \times 10^8/\text{cm}^3$ of the 11-day smoothed NO number density.

partial columns, which have lower uncertainty, that is, higher weighting. The geometric mean of the two slopes is 1.49 (i.e., Halley NO = $\sqrt{1.16 \times (1/0.52)} \times \text{SOFIE NO}$). The Halley NO partial columns are therefore on average 49% higher than those calculated from the SOFIE data set.

Day-to-day differences in NO partial column could arise due to the different sampling of the atmosphere by the two instruments and underestimation of the measurement and data analysis uncertainties. The radiometer makes near-continuous local observations, whereas the satellite data are from solar occultations within the specified geomagnetic zonal range geographically poleward of 60° . Further investigations, ideally with a longer time series of observations than is used in this study, are needed to establish whether NO production in the polar mesosphere and lower thermosphere is enhanced above the Halley region of Antarctica.

The SOFIE daily mean NO number density time series in Figure 6 shows short-term NO production by auroral electron and MEE ionization associated with geomagnetic storms. The NO variability is seen at all altitudes above ~ 65 km but is largest in the lower thermosphere and upper mesosphere. NO number density reaches higher values during the 2013 winter with the $2 \times 10^8/\text{cm}^3$ isopleth descending to ~ 82 km, 10 km lower than for the following winter. The $1 \times 10^8/\text{cm}^3$ isopleth descends to at least 65 km in 2013, ~ 15 km lower than in 2014.

4.3. WACCM-SIC Model Simulation Results

Figure 7 shows the daily mean NO number densities from the WACCM-SIC model simulations for the MEE scenario, calculated for the geomagnetic latitude range -59° to -65° and geographically poleward of 60°S during 2013–2014. Compared to the SOFIE observations (Figure 6) the model simulation shows less short-term

meridional winds showed the opposite behavior in the first half of the 2014 winter with light poleward winds above ~ 75 km and strong equatorward winds below ~ 75 km. Averaged over the altitude range 65–90 km, the 31-day smoothed meridional winds were close to zero throughout both winters. Within the measurement uncertainty there is some indication of light poleward winds in the second half of the 2013 winter, whereas during July 2014 the upper mesospheric wind strengthened slightly in a predominantly equatorward direction.

4.2. Comparison of Radiometer and SOFIE NO Partial Columns

The daily mean NO partial column densities from the ground-based radiometer measurements at Halley are compared in Figure 5 with those calculated by integrating NO number densities observed by SOFIE over altitudes 65–140 km within the geomagnetic latitude range -59° to -65° and geographically poleward of 60°S . Although Figure 5a shows that the general pattern of NO variability is similar for the two data sets, there are significant differences between the measurements (Figure 5b). The largest differences, with Halley partial columns up to $1.0 \times 10^{15}/\text{cm}^2$ higher than the SOFIE values in early 2013 and either side of the 2013 winter solstice, coincide with increased NO and geomagnetic storm activity.

The overlapping Halley ground-based radiometer and SOFIE observations in 2013–2014 are compared further using reduced major axis regression in which the SOFIE and Halley observations are switched as regressors. The linear least squares fits are weighted by the inverse of the variance (i.e., $1/\sigma^2$) for individual NO partial column measurements. The linear regression analyses with the SOFIE observations as regressors, and the Halley data as regressors, are shown in Figures 5c and 5d, respectively. Although there is moderate correlation (coefficient of determination, $R^2 = 0.86$) between the data sets, the regression analyses show rather poor overall agreement. Reduced χ^2 values are 35 and 469, respectively, for the fits using SOFIE and Halley data as regressors. For the latter regression the best fit straight line is biased toward the smaller SOFIE NO partial

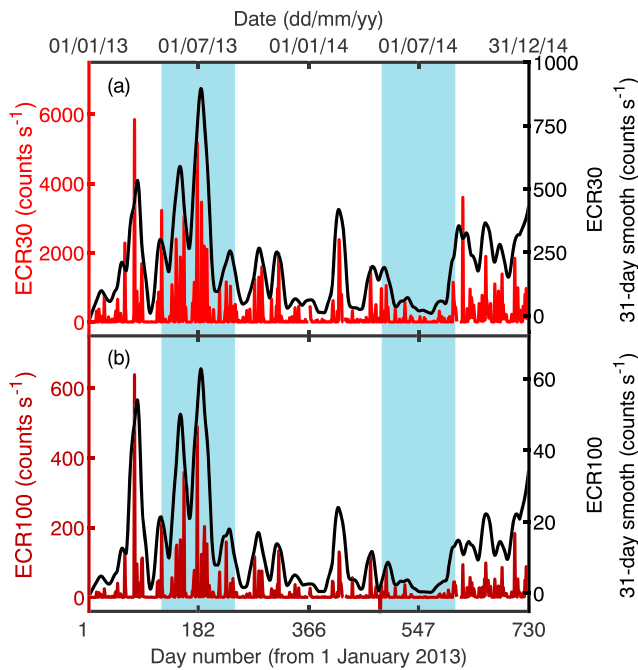


Figure 8. Daily mean and 31-day smoothed POES count rates during 2013–2014 for (a) 30–100 keV electrons (ECR30) and (b) 100–300 keV electrons (ECR100). The POES data are between $L = 3.5$ and 5.5 , equivalent to geomagnetic latitudes 57° – 65° . The shaded light blue areas indicate the months May–August. Note that the daily mean and 31-day smoothed electron count rates are plotted on different scales, shown by the left- and right-hand axes, respectively.

NO variability in the mesosphere and lower thermosphere, but the observed longer-term seasonal variability is reproduced with NO number density increasing at altitudes below 100 km in wintertime. Differences between the MEE and no MEE model runs are shown in Figure 7b where ΔNO , the absolute difference in NO number density, is NO number density (MEE) – NO number density (no MEE). Mesospheric NO number density is generally higher in the MEE run, by up to $3.5 \times 10^7/\text{cm}^3$ compared to the no MEE run at altitudes in the range ~ 55 – 90 km where MEE ionization by 30–1,000 keV electrons is expected to drive NO production. For the MEE run the MEE ionization rates in the model decrease at altitudes above ~ 90 km, with lower direct MEE NO production to augment the auroral, Kp-driven NO production that dominates in the lower thermosphere. Thus, the electron forcing in the two model runs is essentially identical above ~ 90 km.

The daily mean and 31-day smoothed POES-derived count rates for 30–100 keV electrons (ECR30) and 100–300 keV electrons (ECR100) are shown in Figure 8. These data further highlight the large differences in MEE forcing during the two years, in particular during the winter periods with much higher MEE fluxes observed in 2013. The NO partial columns and number density from the observations and, to a certain extent in the model simulations, increase when sustained high MEE count rates occur.

The differences between the two WACCM-SIC runs are very similar to those reported for WACCM simulations over decadal timescales (Andersson et al., 2018) as well as for WACCM simulations over decadal timescales (Andersson et al., 2018) rather than the electron observation-based estimates of MEE ionization used in this study. For the polar SH (geographic latitude range 60° – 90°S) the Andersson et al. (2018) model calculations show the largest relative increases in NO_x during

the summer, exceeding 200% at altitudes ~ 75 – 90 km. During mid-winter the Ap index-driven MEE ionization increased average mesospheric NO_x by over 20%.

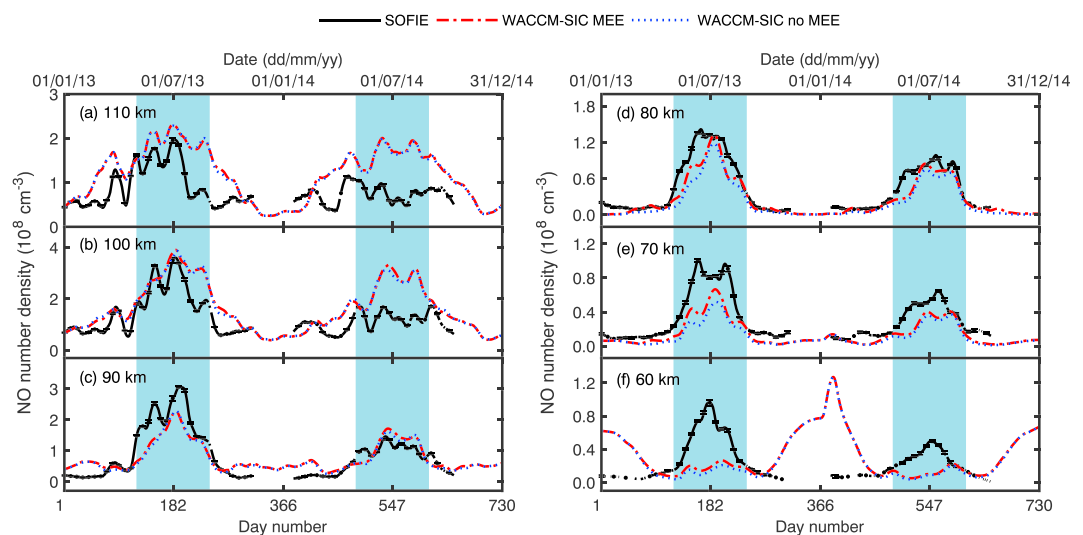


Figure 9. Comparison of 31-day smoothed SOFIE NO number density observations and the corresponding model data from WACCM-SIC runs with and without MEE ionization. The data are at discrete 10 km levels descending from 110 km to 60 km. Observation and model data are restricted to the geomagnetic latitude range -59° to -65° and geographically poleward of 60°S . The error bars on the SOFIE data are $\pm 1\sigma$. The shaded light blue panels indicate the months May–August.

4.4. Comparison of Observed NO Number Density With Model Simulations

The SOFIE observations and WACCM-SIC simulation results are compared in Figure 9, which shows NO number density at 10 km intervals from 60 to 110 km after applying a 31-day moving average to each of the three data sets. Smoothing reveals the general long-term and seasonal differences between the data sets by removing the large day-to-day differences between the two model runs arising from short-term NO variability. The largest differences between the smoothed MEE and no MEE model data are at 60, 70, and 80 km during the 2013 winter with the smoothed MEE NO number density up to $2.7 \times 10^7/\text{cm}^3$ higher. At higher altitudes the results for the two model runs are very similar due to the electron forcing in the two model runs being essentially identical above ~ 90 km. The best agreement between the SOFIE observations and MEE model data is at 80 km, although the model does not reproduce observed NO number density increases during the first half of each winter. The modeled NO number density reaches a maximum close to midwinter in 2013, higher than is reached in 2014. The observed wintertime NO at 80 km and below is almost always higher than in the MEE model run. At 60 km the observed NO number density is up to $0.8 \times 10^8/\text{cm}^3$ higher than the model in both years at midwinter. However, at altitudes in the range 90–110 km this discrepancy switches round with modeled NO number density generally higher than is observed, and up to $1.9 \times 10^8/\text{cm}^3$ higher than the observations close to midwinter. This suggests that the auroral forcing in WACCM-SIC could be too high or that the rate of downward transport of NO produced in the lower thermosphere is too low in the model.

5. Discussion

Our WACCM-SIC calculations combine, for the first time in a 3-D global atmospheric model, the most detailed representation of *D*-region ion-neutral chemistry with MEE ionization rates estimated from electron flux observations. By including these additional components in the simulations, modeled NO number density in the mesosphere is increased, and there is closer agreement with observations for the upper mesosphere (altitudes ~ 70 – 90 km). However, there remain significant quantitative differences between modeled NO distributions and those observed during 2013–2014, in particular for the lower mesosphere (~ 50 – 70 km) and lower thermosphere (≥ 90 km). Various possible factors are discussed, which could produce these discrepancies between the observations and model results. These factors include the derivation and accuracy of the used MEE ionization rates, the characterization of NO downward transport in the model, and uncertainties in lower thermospheric NO production mechanisms.

The MEE ionization rates used in the simulations are based on a model of 30–1000 keV energetic electron precipitation constructed using observations from the POES MEPED satellite during 2013–2014. POES observations in and around the SAA are seriously affected by proton contamination (Rodger et al., 2013), that cannot be readily removed or corrected, and these regional data are not included in the zonally averaged model. The SAA corresponds to the drift loss cone region where electron fluxes into the atmosphere are expected to be considerably higher. This could result in an underestimation of MEE ionization rates, perhaps by a factor 2–3, in the simulations over a large region of the SH mesosphere.

The Prandtl number (*Pr*) is the ratio of momentum diffusivity to thermal diffusivity, which affects atmospheric transport and NO distributions. The eddy diffusion coefficient (*K_{zz}*) in WACCM is a product of the gravity wave drag parameterization (Garcia et al., 2007) and is proportional to the gravity wave drag and inversely proportional to the Prandtl number. Our WACCM-SIC model simulations were run with enhanced *K_{zz}*, produced by setting *Pr* to 2. A control run with *Pr* = 4 reduced mesospheric NO volume mixing ratio throughout the two-year period 2013–2014, as expected due to weaker downward transport using the standard eddy diffusion rate, but also slightly decreased thermospheric NO. Setting the Prandtl number below the recommended value of 2 increased mesospheric NO in our WACCM-SIC simulations, producing better agreement between the modeled and observed data for both winters and also increased thermospheric NO abundance.

Hendrickx et al. (2018) compared seven years (2007–2015) of SOFIE NO observations in the SH with simulations performed by the standard version of WACCM incorporating SD. SD-WACCM includes a *K_p*-driven auroral electron parameterization but lacks the specific *D*-region ion-neutral chemistry and MEE precipitation that are in WACCM-SIC. However, above the mesopause MEE precipitation has a negligible effect, and similar to our findings using WACCM-SIC, their modeled NO concentrations in the lower thermosphere are almost a factor 2 higher than observations. Hendrickx et al. (2018) suggest that the differences between their

observations and model simulations could be attributed, at least in part, to uncertainties and challenges in determining reaction rates and branching ratios in several NO reactions involving excited state ($N(^2D)$) and ground state ($N(^4S)$) nitrogen. In the standard parameterization in WACCM (Jackman et al., 2005; Marsh et al., 2007) an ion pair produces 1.25 N atoms with branching ratios of 0.55 $N(^4S)$ and 0.70 $N(^2D)$. However, as pointed out by Hendrickx et al. (2018), other recommended values of the $N(^2D)$ branching ratio range from 0.50 to 0.60 (Solomon et al., 1982; Yonker, 2013). Our simulations use a different parameterization from standard WACCM, with the detailed and verified mechanisms implemented in WACCM-SIC (Kovács et al., 2016) based on comprehensive analysis and revision of the *D*-region chemistry in the SIC model using updated rate coefficients (Pavlov, 2014; Verronen et al., 2016). However, the significant discrepancies found between modeled and observed NO using either standard WACCM or WACCM-SIC indicate that further studies may be needed to verify the reaction parameterizations for the critical pathways that impact mesospheric and lower thermospheric NO production and loss.

6. Conclusions

NO in the mesosphere and lower thermosphere above Antarctica has been studied during a two-year period, 2013–2014, close to solar maximum. Contrasting levels of geomagnetic storm activity occurred during the two austral winters, with nine moderate geomagnetic storms (minimum *Dst* index ≤ -50 nT) during May–August in 2013 compared to just one storm at the start and one close to the end of the corresponding period in 2014. The geomagnetic storms caused energetic electron precipitation into the polar middle atmosphere, driving NO production in the mesosphere, and lower thermosphere. Energetic electron measurements by the 0° electron telescope on the POES SEM-2 MEPED instrument over $L = 3.5$ – 5.5 (geomagnetic latitudes $\sim 57^\circ$ – 65°), corrected for proton contamination, show much higher count rates for 30–300 keV electrons during the 2013 winter compared to 2014.

Ground-based measurements from Halley, Antarctica ($L = 4.7$, geomagnetic latitude -62°), of daily mean NO partial column densities at altitudes above ~ 65 km using passive millimeter-wave radiometry show significant differences (up to $1.0 \times 10^{15}/\text{cm}^2$ higher for the Halley measurements) compared to satellite observations over 65–140 km by the SOFIE instrument. The differences in partial column could be due to higher NO abundance in the region of the Antarctic mesosphere and lower thermosphere above Halley and underestimated measurement uncertainties. Short-term increases in mesospheric and lower thermospheric NO, observed by both instruments, coincided with moderate geomagnetic storm occurrences, increases in ionization at ~ 75 – 90 km observed by the Halley riometer, and increased MEPED electron count rates. During the 2013 winter, NO number density was up to $3 \times 10^8/\text{cm}^3$ higher than in the corresponding period of 2014, suggesting greater MEE production directly in the mesosphere and lower thermosphere in 2013. However, radar measurements show distinctly different behavior of the zonal and meridional mesospheric wind components above Halley, in particular after midwinter in the two years. This contrast in wintertime horizontal winds indicates differing localized dynamical conditions that if present over a more widespread region of the SH polar middle atmosphere could also potentially affect NO distributions.

WACCM-SIC simulations show that including full *D*-region ion-neutral chemistry and estimates of MEE ionization in the 3-D model increases calculated NO number density in the high-latitude SH winter mesosphere by up to $3.5 \times 10^7/\text{cm}^3$. However, the model still significantly underestimates NO in the wintertime mesosphere, whereas lower thermospheric levels are much higher than observed. This underestimation of mesospheric NO abundance could be resolved by increasing MEE ionization rates in the model to boost direct NO production at 55–90 km or more efficient transport of NO from the lower thermosphere to the lower mesosphere. Our results provide further evidence in support of other recent studies that identify the need to further refine our understanding of MEE processes in the polar middle atmosphere. The impact of uncertainties in branching and ionization rates and vertical transport parameterizations on modeled NO distributions needs to be further investigated, and further observational data for NO_x and HO_x species are needed to verify and develop the models.

References

- Andersson, M. E., Verronen, P. T., Marsh, D. R., Päiväranta, S.-M., & Plane, J. M. C. (2016). WACCM-D—Improved modeling of nitric acid and active chlorine during energetic particle precipitation. *Journal of Geophysical Research: Atmospheres*, 121, 10,328–10,341. <https://doi.org/10.1002/2015JD024173>

Acknowledgments

This work was supported in part by the UK Natural Environment Research Council (grant references NE/J022187/1 and NE/J02077X/1) and the Marsden Fund. A. S. was supported by the Academy of Finland (projects 258165 and 265005). The work of P. T. Verronen and M. E. Andersson was supported by the Academy of Finland (project 276926 - SECTIC: Sun-Earth Connection Through Ion Chemistry). L. M. was supported by the Swedish Research Council under contract 621-2012-1648. D. R. M. was supported in part by NASA Living With a Star grant NNX14AH54G. The National Center for Atmospheric Research (NCAR) is sponsored by the U.S. National Science Foundation (NSF). We thank Christoph Larndorfer, William Clark, David Maxfield, Jonas Ekstedt, and Paul Breen for supporting the observations at Halley, Antarctica. We thank Anne K. Smith for providing the SD-WACCM data and Martyn Chipperfield for helpful discussions. Aaron Hendry is acknowledged for providing computer code (GEO2CGM) to facilitate the conversion from spherical geographic coordinates to spherical corrected geomagnetic coordinates. Data from the WACCM-SIC runs are archived at the University of Leeds. Observational data sets from Halley, Antarctica, are available from the UK Polar Data Centre (<https://www.bas.ac.uk/data/uk-pdc/>).

- Andersson, M. E., Verronen, P. T., Marsh, D. R., Seppälä, A., Päivärinta, S.-M., Rodger, C. J., & van de Kamp, M. (2018). Polar ozone response to energetic particle precipitation over decadal time scales: The role of medium-energy electrons. *Journal of Geophysical Research: Atmospheres*, *123*, 607–622. <https://doi.org/10.1002/2017JD027605>
- Andersson, M. E., Verronen, P. T., Rodger, C. J., Clilverd, M. A., & Seppälä, A. (2014). Missing driver in the Sun–Earth connection from energetic electron precipitation impacts mesospheric ozone. *Nature Communications*, *5*(1), 5197. <https://doi.org/10.1038/ncomms6197>
- Andersson, M. E., Verronen, P. T., Rodger, C. J., Clilverd, M. A., & Wang, S. (2014). Longitudinal hotspots in the mesospheric OH variations due to energetic electron precipitation. *Atmospheric Chemistry and Physics*, *14*(2), 1095–1105. <https://doi.org/10.5194/acp-14-1095-2014>
- Andersson, M. E., Verronen, P. T., Wang, S., Rodger, C. J., Clilverd, M. A., & Carson, B. R. (2012). Precipitating radiation belt electrons and enhancements of mesospheric hydroxyl during 2004–2009. *Journal of Geophysical Research*, *117*, D09304. <https://doi.org/10.1029/2011JD017246>
- Arsenovic, P., Rozanov, E., Stenke, A., Funke, B., Wissing, J. M., & Mursula, et al. (2016). The influence of middle range energy electrons on atmospheric chemistry and regional climate. *Journal of Atmospheric and Solar-Terrestrial Physics*, *149*, 180–190. <https://doi.org/10.1016/j.jastp.2016.04.008>
- Baumgaertner, A. J. G., Seppälä, A., Jöckel, P., & Clilverd, M. A. (2011). Geomagnetic activity related NO_x enhancements and polar surface air temperature variability in a chemistry climate model: Modulation of the NAM index. *Atmospheric Chemistry and Physics*, *11*(9), 4521–4531. <https://doi.org/10.5194/acp-11-4521-2011>
- Brasseur, G. P., & Solomon, S. (2005). *Aeronomy of the middle atmosphere*, (3rd ed.). Dordrecht, Netherlands: Springer.
- Briggs, B. H. (1984). The analysis of spaced sensor records by correlation techniques. In International Council of Scientific Unions Middle Atmosphere Program (MAP) Handbook, 13, pp. 166–186 (SEE N85-17452 08-46).
- Clilverd, M. A., Seppälä, A., Rodger, C. J., Mlynzcak, M. G., & Kozyra, J. U. (2009). Additional stratospheric NO_x production by relativistic electron precipitation during the 2004 spring NO_x descent event. *Journal of Geophysical Research*, *114*, A04305. <https://doi.org/10.1029/2008JA013472>
- Clilverd, M. A., Seppälä, A., Rodger, C. J., Thomson, N. R., Lichtenberger, J., & Steinbach, P. (2007). Temporal variability of the descent of high-altitude NO_x inferred from ionospheric data. *Journal of Geophysical Research*, *112*, A09307. <https://doi.org/10.1029/2006JA012085>
- Daae, M., Espy, P., Nesse Tyssøy, H., Newnham, D., Stadsnes, J., & Søråas, F. (2012). The effect of energetic electron precipitation on middle mesospheric night-time ozone during and after a moderate geomagnetic storm. *Geophysical Research Letters*, *39*, L21811. <https://doi.org/10.1029/2012GL053787>
- Espy, P. J., Hartogh, P., & Holmen, K. (2006). A microwave radiometer for the remote sensing of nitric oxide and ozone in the middle atmosphere. *Proceedings of SPIE*, *6362*, 63620P1–63620P9. <https://doi.org/10.1117/12.688953>
- Evans, D. S., & Greer, M. S. (2004). Polar orbiting environmental satellite space environment monitor—2 instrument descriptions and archive data documentation. NOAA Technical Memorandum version 1.4, Space Environment Laboratory, Boulder, Colo.
- Eyring, V., Lamarque, J.-F., Hess, P., Arfeuille, F., Bowman, K., Chipperfield, M. P., et al. (2013). Overview of IGAC/SPARC Chemistry Climate Model Initiative (CCMI) community simulations in support of upcoming ozone and climate assessments. *SPARC Newsletter*, *40*, 48–66.
- Fang, X., Randall, C. E., Lummerzheim, D., Wang, W., Lu, G., Solomon, S. C., & Frahm, R. A. (2010). Parameterization of monoenergetic electron impact ionization. *Geophysical Research Letters*, *37*, L22106. <https://doi.org/10.1029/2010GL045406>
- Funke, B., Ball, W., Bender, S., Gardini, A., Harvey, V. L., Lambert, A., et al. (2017). HEPPA-II model–measurement intercomparison project: EPP indirect effects during the dynamically perturbed NH winter 2008–2009. *Atmospheric Chemistry and Physics*, *17*(5), 3573–3604. <https://doi.org/10.5194/acp-17-3573-2017>
- Garcia, R. R., Manuel, L., Funke, B., Marsh, D. R., Kinnison, D. E., Smith, A. K., & Francisco, G. (2014). On the distribution of CO₂ and CO in the mesosphere and lower thermosphere. *Journal of Geophysical Research: Atmospheres*, *119*, 5700–5718. <https://doi.org/10.1002/2013jd021208>
- Garcia, R. R., Marsh, D. R., Kinnison, D. E., Boville, B. A., & Sassi, F. (2007). Simulation of secular trends in the middle atmosphere 1950–2003. *Journal of Geophysical Research*, *112*, D09301. <https://doi.org/10.1029/2006JD007485>
- Gómez-Ramírez, D., McNabb, J. W. C., Russell, J. M., Hervig, M. E., Deaver, L. E., Paxton, G., & Bernath, P. F. (2013). Empirical correction of thermal responses in the Solar Occultation for Ice Experiment nitric oxide measurements and initial data validation results. *Applied Optics*, *52*(13), 2950–2959. <https://doi.org/10.1364/AO.52.002950>
- Gordley, L. L., Hervig, M. E., Fish, C., Russell, J. M. III, Cook, J., Hanson, S., et al. (2009). The Solar Occultation For Ice Experiment (SOFIE). *Journal of Atmospheric and Solar-Terrestrial Physics*, *71*(3-4), 300–315. <https://doi.org/10.1016/j.jastp.2008.07.012>
- Hartogh, P., & Hartmann, G. K. (1990). A high-resolution chirp transform spectrometer for microwave measurements. *Measurement Science and Technology*, *1*(7), 592–595. <https://doi.org/10.1088/0957-0233/1/7/008>
- Harvey, V. L., Pierce, R. B., Hitchman, M. H., Randall, C. E., & Fairlie, T. D. (2004). On the distribution of ozone in stratospheric anticyclones. *Journal of Geophysical Research*, *109*, D24308. <https://doi.org/10.1029/2004JD004992>
- Hendrickx, K., Megner, L., Gumbel, J., Siskind, D. E., Orsolini, Y. J., Nesse Tyssøy, H., & Hervig, M. (2015). Observations of 27 day solar cycles in the production and mesospheric descent of EPP-produced NO. *Journal of Geophysical Research: Space Physics*, *120*, 8978–8988. <https://doi.org/10.1002/2015JA021441>
- Hendrickx, K., Megner, L., Marsh, D. R., Gumbel, J., Strandberg, R., & Martinsson, F. (2017). Relative importance of nitric oxide physical drivers in the lower thermosphere. *Geophysical Research Letters*, *44*, 10,081–10,087. <https://doi.org/10.1002/2017GL074786>
- Hendrickx, K., Megner, L., Marsh, D. R., & Smith-Johnsen, C. (2018). Production and transport mechanisms of NO in observations and models. *Atmospheric Chemistry and Physics Discussions*, 1–24. <https://doi.org/10.5194/acp-2017-1188>, in review.
- Hendry, A. T., Rodger, C. J., & Clilverd, M. A. (2017). Evidence of sub-MeV EMIC-driven electron precipitation. *Geophysical Research Letters*, *44*, 1210–1218. <https://doi.org/10.1002/2016GL071807>
- Hibbins, R. E., Shanklin, J. D., Espy, P. J., Jarvis, M. J., Riggan, D. M., Fritts, D. C., & Lübken, F.-J. (2005). Seasonal variations in the horizontal wind structure from 0–100 km above Rothera station, Antarctica (67° S, 68° W). *Atmospheric Chemistry and Physics*, *5*(11), 2973–2980. <https://doi.org/10.5194/acp-5-2973-2005>
- Horne, R. B., Lam, M. M., & Green, J. C. (2009). Energetic electron precipitation from the outer radiation belt during geomagnetic storms. *Geophysical Research Letters*, *36*, L19104. <https://doi.org/10.1029/2009GL040236>
- Horne, R. B., Thorne, R. M., Shprits, Y. Y., Meredith, N. P., Glauert, S. A., Smith, A. J., et al. (2005). Wave acceleration of electrons in the Van Allen radiation belts. *Nature*, *437*(7056), 227–230. <https://doi.org/10.1038/nature03939>
- Isono, Y., Mizuno, A., Nagahama, T., Miyoshi, Y., Nakamura, T., Kataoka, R., et al. (2014a). Variations of nitric oxide in the mesosphere and lower thermosphere over Antarctica associated with a magnetic storm in April 2012. *Geophysical Research Letters*, *41*, 2568–2574. <https://doi.org/10.1002/2014GL059360>

- Isono, Y., Mizuno, A., Nagahama, T., Miyoshi, Y., Nakamura, T., Kataoka, R., et al. (2014b). Ground-based observations of nitric oxide in the mesosphere and lower thermosphere over Antarctica in 2012–2013. *Journal of Geophysical Research: Space Physics*, *119*, 7745–7761. <https://doi.org/10.1002/2014JA019881>
- Jackman, C. H., DeLand, M. T., Labow, G. J., Fleming, E. L., Weisenstein, D. K., Ko, M. K. W., et al. (2005). Neutral atmospheric influences of the solar proton events in October–November 2003. *Journal of Geophysical Research*, *110*, A09S27. <https://doi.org/10.1029/2004JA010888>
- Jackman, C. H., Marsh, D. R., Vitt, F. M., Garcia, R. R., Randall, C. E., Fleming, E. L., & Frith, S. M. (2009). Long-term middle atmospheric influence of very large solar proton events. *Journal of Geophysical Research*, *114*, D11304. <https://doi.org/10.1029/2008JD011415>
- Jackman, C. H., & McPeters, R. D. (2004). The effect of solar proton events on ozone and other constituents. In *Solar variability and its effects on climate, Geophysical Monograph Series* (Vol. 141, pp. 305–319). Washington, DC: American Geophysical Union. <https://doi.org/10.1029/141GM21>
- Janssen, M. A. (Ed.) (1993). *Atmospheric remote sensing by microwave radiometry*. New York: Wiley-Blackwell.
- Kirkwood, S., Osepian, A., Belova, E., Urban, J., Pérot, K., & Sinha, A. K. (2015). Ionization and NO production in the polar mesosphere during high-speed solar wind streams: Model validation and comparison with NO enhancements observed by Odin-SMR. *Annales Geophysicae*, *33*(5), 561–572. <https://doi.org/10.5194/angeo-33-561-2015>
- Kovács, T., Plane, J. M. C., Feng, W., Nagy, T., Chipperfield, M. P., Verronen, P. T., et al. (2016). D-region ion–neutral coupled chemistry (Sodankylä Ion Chemistry, SIC) within the Whole Atmosphere Community Climate Model (WACCM 4) – WACCM-SIC and WACCM-rSIC. *Geoscientific Model Development*, *9*(9), 3123–3136. <https://doi.org/10.5194/gmd-9-3123-2016>
- Krishnaswamy, S., Detrick, D. L., & Rosenberg, T. J. (1985). The inflection point method of determining riometer quiet day curves. *Radio Science*, *20*(1), 123–136. <https://doi.org/10.1029/RS020i001p00123>
- Lam, M. M., Horne, R. B., Meredith, N. P., Glauert, S. A., Moffat-Griffin, T., & Green, J. C. (2010). Origin of energetic electron precipitation >30 keV into the atmosphere. *Journal of Geophysical Research*, *115*, A00F08. <https://doi.org/10.1029/2009JA014619>
- Lee, J. N., Wu, D. L., Manney, G. L., Schwartz, M. J., Lambert, A., Livesey, N. J., et al. (2011). Aura Microwave Limb Sounder observations of the polar middle atmosphere: Dynamics and transport of CO and H₂O. *Journal of Geophysical Research*, *116*, D05110. <https://doi.org/10.1029/2010JD014608>
- Little, C. G., & Leinbach, H. (1959). The riometer—A device for the continuous measurement of ionospheric absorption. *Proceedings of the IRE*, *47*, 315–320. <https://doi.org/10.1109/JRPROC.1959.287299>
- Mann, G. W., Anderson, P. S., & Mobbs, S. D. (2000). Profile measurements of blowing snow at Halley, Antarctica. *Journal of Geophysical Research: Atmospheres*, *105*(D19), 24,491–24,508. <https://doi.org/10.1029/2000JD900247>
- Marsh, D. R., Garcia, R. R., Kinnison, D. E., Boville, B. A., Sassi, F., Solomon, S. C., & Matthes, K. (2007). Modeling the whole atmosphere response to solar cycle changed in radiative and geomagnetic forcing. *Journal of Geophysical Research*, *112*, D23306. <https://doi.org/10.1029/2006JD008306>
- Marsh, D. R., Mills, M. J., Kinnison, D. E., & Lamarque, J.-F. (2013). Climate change from 1850 to 2005 simulated in CESM1 (WACCM). *Journal of Climate*, *26*(19), 7372–7391. <https://doi.org/10.1175/JCLI-D-12-00558.1>
- Marsh, D. R., Solomon, S. C., & Reynolds, A. E. (2004). Empirical model of nitric oxide in the lower thermosphere. *Journal of Geophysical Research*, *109*, A07301. <https://doi.org/10.1029/2003JA010199>
- Matthes, K., Funke, B., Andersson, M. E., Barnard, L., Beer, J., Charbonneau, P., et al. (2017). Solar forcing for CMIP6 (v3.2). *Geoscientific Model Development*, *10*(6), 2247–2302. <https://doi.org/10.5194/gmd-10-2247-2017>
- Mironova, I. A., Aplin, K. L., Arnold, F., Bazilevskaya, G. A., Harrison, R. G., Krivolutsky, A. A., et al. (2015). Energetic particle influence on the Earth's atmosphere. *Space Science Reviews*, *194*(1–4), 1–96. <https://doi.org/10.1007/s11214-015-0185-4>
- Newnham, D. A., Espy, P. J., Clilverd, M. A., Rodger, C. J., Seppälä, A., Maxfield, D. J., et al. (2011). Direct observations of nitric oxide produced by energetic electron precipitation into the Antarctic middle atmosphere. *Geophysical Research Letters*, *38*, L20104. <https://doi.org/10.1029/2011GL048666>
- Newnham, D. A., Espy, P. J., Clilverd, M. A., Rodger, C. J., Seppälä, A., Maxfield, D. J., et al. (2013). Observations of nitric oxide in the Antarctic middle atmosphere during recurrent geomagnetic storms. *Journal of Geophysical Research: Space Physics*, *118*, 7874–7885. <https://doi.org/10.1002/2013JA019056>
- Orsolini, Y. J., Smith-Johnsen, C., Marsh, D. R., Stordal, F., Rodger, C. J., Verronen, P. T., & Clilverd, M. A. (2018). Mesospheric nitric acid enhancements during energetic electron precipitation events simulated by WACCM-D. *Journal of Geophysical Research: Atmospheres*, *123*. <https://doi.org/10.1029/2017JD028211>
- Pavlov, A. V. (2014). Photochemistry of ions at D-region altitudes of the ionosphere: A review. *Surveys in Geophysics*, *35*(2), 259–334. <https://doi.org/10.1007/s10712-013-9253-z>
- Randall, C. E., Harvey, V. L., Singleton, C. S., Bailey, S. M., Bernath, P. F., Codrescu, M., et al. (2007). Energetic particle precipitation effects on the southern hemisphere stratosphere in 1992–2005. *Journal of Geophysical Research*, *112*, D08308. <https://doi.org/10.1029/2006JD007696>
- Randall, C. E., Harvey, V. L., Siskind, D. E., France, J., Bernath, P. F., Boone, C. D., & Walker, K. A. (2009). NO_x descent in the Arctic middle atmosphere in early 2009. *Geophysical Research Letters*, *36*, L18811. <https://doi.org/10.1029/2009GL039706>
- Rees, M. H. (1989). *Physics and chemistry of the upper atmosphere, Cambridge Atmospheric and Space Science Series*. (). Cambridge, UK: Cambridge University Press. <https://doi.org/10.1017/CBO9780511573118>
- Rienecker, M. M., Suarez, M. J., Gelaro, R., Todling, R., Bacmeister, J., Liu, E., et al. (2011). MERRA: NASA's Modern-Era Retrospective Analysis for Research and Applications. *Journal of Climate*, *24*(14), 3624–3648. <https://doi.org/10.1175/JCLI-D-11-00015.1>
- Rodger, C. J., Clilverd, M. A., Green, J. C., & Lam, M. M. (2010). Use of POES SEM-2 observations to examine radiation belt dynamics and energetic electron precipitation into the atmosphere. *Journal of Geophysical Research*, *115*, A04202. <https://doi.org/10.1029/2008JA014023>
- Rodger, C. J., Clilverd, M. A., Kavanagh, A. J., Watt, C. E. J., Verronen, P. T., & Raita, T. (2012). Contrasting the responses of three different ground-based instruments to energetic electron precipitation. *Radio Science*, *47*, RS2021. <https://doi.org/10.1029/2011RS004971>
- Rodger, C. J., Kavanagh, A. J., Clilverd, M. A., & Marple, S. (2013). Comparison between POES energetic electron precipitation observations and riometer absorptions: Implications for determining true precipitation fluxes. *Journal of Geophysical Research: Space Physics*, *118*, 7810–7821. <https://doi.org/10.1002/2013JA019439>
- Ryan, N. J., Kinnison, D. E., Garcia, R. R., Hoffmann, C. G., Palm, M., Raffalski, U., & Notholt, J. (2018). Assessing the ability to derive rates of polar middle-atmospheric descent using trace gas measurements from remote sensors. *Atmospheric Chemistry and Physics*, *18*(3), 1457–1474. <https://doi.org/10.5194/acp-18-1457-2018>
- Sandford, D. J., Beldon, C. L., Hibbins, R. E., & Mitchell, N. J. (2010). Dynamics of the Antarctic and Arctic mesosphere and lower thermosphere—Part 1: Mean winds. *Atmospheric Chemistry and Physics*, *10*(21), 10,273–10,289. <https://doi.org/10.5194/acp-10-10273-2010>

- Semeniuk, K., Fomichev, V. I., McConnell, J. C., Fu, C., Melo, S. M. L., & Usoskin, I. G. (2011). Middle atmosphere response to the solar cycle in irradiance and ionizing particle precipitation. *Atmospheric Chemistry and Physics*, 11(10), 5045–5077. <https://doi.org/10.5194/acp-11-5045-2011>
- Seppälä, A., Lu, H., Clilverd, M. A., & Rodger, C. J. (2013). Geomagnetic activity signatures in wintertime stratosphere wind, temperature, and wave response. *Journal of Geophysical Research: Atmospheres*, 118, 2169–2183. <https://doi.org/10.1002/jgrd.50236>
- Seppälä, A., Randall, C. E., Clilverd, M. A., Rozanov, E., & Rodger, C. J. (2009). Geomagnetic activity and polar surface air temperature variability. *Journal of Geophysical Research*, 114, A10312. <https://doi.org/10.1029/2008JA014029>
- Sheese, P. E., Gattinger, R. L., Llewellyn, E. J., Boone, C. D., & Strong, K. (2011). Nighttime nitric oxide densities in the southern hemisphere mesosphere–lower thermosphere. *Geophysical Research Letters*, 38, L15812. <https://doi.org/10.1029/2011GL048054>
- Shimazaki, T. (1984). The photochemical time constants of minor constituents and their families in the middle atmosphere. *Journal of Atmospheric and Terrestrial Physics*, 46(2), 173–191. [https://doi.org/10.1016/0021-9169\(84\)90143-0](https://doi.org/10.1016/0021-9169(84)90143-0)
- Sinnhuber, M., Funke, B., von Clarmann, T., Lopez-Puertas, M., Stiller, G. P., & Seppälä, A. (2014). Variability of NO_x in the polar middle atmosphere from October 2003 to March 2004: Vertical transport vs. local production by energetic particles. *Atmospheric Chemistry and Physics*, 14(14), 7681–7692. <https://doi.org/10.5194/acp-14-7681-2014>
- Sinnhuber, M., Nieder, H., & Wieters, N. (2012). Energetic particle precipitation and the chemistry of the mesosphere/lower thermosphere. *Surveys in Geophysics*, 33(6), 1281–1334. <https://doi.org/10.1007/s10712-012-9201-3>
- Siskind, D. E., Nedoluha, G. E., Randall, C. E., Fromm, M., & Russell, J. M. III (2000). An assessment of southern hemisphere stratospheric NO_x enhancements due to transport from the upper atmosphere. *Geophysical Research Letters*, 27(3), 329–332. <https://doi.org/10.1029/1999GL010940>
- Smith, A. K. (2012). Global dynamics of the MLT. *Surveys in Geophysics*, 33(6), 1177–1230. <https://doi.org/10.1007/s10712-012-9196-9>
- Smith, A. K., Garcia, R. R., Marsh, D. R., & Richter, J. H. (2011). WACCM simulations of the mean circulation and trace species transport in the winter mesosphere. *Journal of Geophysical Research*, 116, D20115. <https://doi.org/10.1029/2011JD016083>
- Smith-Johnsen, C., Nesse Tyssøy, H., Hendrickx, K., Orsolini, Y., Kishore Kumar, G., Ødegaard, L.-K. G., et al. (2017). Direct and indirect electron precipitation effect on nitric oxide in the polar middle atmosphere, using a full-range energy spectrum. *Journal of Geophysical Research: Space Physics*, 122, 8679–8693. <https://doi.org/10.1002/2017JA024364>
- Solomon, S., Crutzen, P. J., & Roble, R. G. (1982). Photochemical coupling between the thermosphere and the lower atmosphere: 1. Odd nitrogen from 50 to 120 km. *Journal of Geophysical Research*, 87(C9), 7206–7220. <https://doi.org/10.1029/JC087iC09p07206>
- Solomon, S. C., Barth, C. A., & Bailey, S. M. (1999). Auroral production of nitric oxide measured by the SNOE satellite. *Geophysical Research Letters*, 26(9), 1259–1262. <https://doi.org/10.1029/1999GL000235>
- Søråas, F., Sandanger, M. I., & Smith-Johnsen, C. (2017). NOAA POES and MetOp particle observations during the 17 March 2013 storm. *Journal of Atmospheric and Solar-Terrestrial Physics*. <https://doi.org/10.1016/j.jastp.2017.09.004>
- Thébault, E., Finlay, C. C., Beggan, C. D., Alken, P., Aubert, J., Barrois, O., et al. (2015). International Geomagnetic Reference Field: The 12th generation. *Earth, Planets and Space*, 67(1), 1–19. <https://doi.org/10.1186/s40623-015-0228-9>
- Turunen, E., Verronen, P. T., Seppälä, A., Rodger, C. J., Clilverd, M. A., Tamminen, J., et al. (2009). Impact of different precipitation energies on NO_x generation during geomagnetic storms. *Journal of Atmospheric and Solar-Terrestrial Physics*, 71(10–11), 1176–1189. <https://doi.org/10.1016/j.jastp.2008.07.005>
- van de Kamp, M., Seppälä, A., Clilverd, M. A., Rodger, C. J., Verronen, P. T., & Whittaker, I. C. (2016). A model providing long-term data sets of energetic electron precipitation during geomagnetic storms. *Journal of Geophysical Research: Atmospheres*, 121, 12,520–12,540. <https://doi.org/10.1002/2015JD024212>
- Verronen, P. T., Andersson, M. E., Marsh, D. R., Kovács, T., & Plane, J. M. C. (2016). WACCM-D - Whole Atmosphere Community Climate Model with D-region ion chemistry. *Journal of Advances in Modeling Earth Systems*, 8, 954–975. <https://doi.org/10.1002/2015MS000592>
- Verronen, P. T., Andersson, M. E., Rodger, C. J., Clilverd, M. A., Wang, S., & Turunen, E. (2013). Comparison of modeled and observed effects of radiation belt electron precipitation on mesospheric hydroxyl and ozone. *Journal of Geophysical Research: Atmospheres*, 118, 11,419–11,428. <https://doi.org/10.1002/jgrd.50845>
- Verronen, P. T., Rodger, C. J., Clilverd, M. A., & Wang, S. (2011). First evidence of mesospheric hydroxyl response to electron precipitation from the radiation belts. *Journal of Geophysical Research*, 116, D07307. <https://doi.org/10.1029/2010JD014965>
- Verronen, P. T., Seppälä, A., Clilverd, M. A., Rodger, C. J., Kyrölä, E., Enell, C.-F., et al. (2005). Diurnal variation of ozone depletion during the October–November 2003 solar proton events. *Journal of Geophysical Research*, 110, A09S32. <https://doi.org/10.1029/2004JA010932>
- Villanueva, G., & Hartogh, P. (2004). The high resolution chirp transform spectrometer for the SOFIA-GREAT instrument. *Experimental Astronomy*, 18(1–3), 77–91. <https://doi.org/10.1007/s10686-005-9004-3>
- Villanueva, G. L., Hartogh, P., & Reindl, L. (2006). A digital dispersive matching network for SAW devices in chirp transform spectrometers. *IEEE Transactions on Microwave Theory and Techniques*, 54(4), 1415–1424. <https://doi.org/10.1109/TMTT.2006.871244>
- Webb, D. F., & Howard, T. A. (2012). Coronal mass ejections: Observations. *Living Reviews in Solar Physics*, 9(3). <https://doi.org/10.12942/lrsp-2012-3>
- Whittaker, I. C., Gamble, R. J., Rodger, C. J., Clilverd, M. A., & Sauvaud, J.-A. (2013). Determining the spectra of radiation belt electron losses: Fitting DEMETER electron flux observations for typical and storm times. *Journal of Geophysical Research: Space Physics*, 118, 7611–7623. <https://doi.org/10.1002/2013JA019228>
- Winkler, H., Sinnhuber, M., Notholt, J., Kallenrode, M.-B., Steinhilber, F., Vogt, J., et al. (2008). Modelling impacts of geomagnetic field variations on middle atmospheric ozone responses to solar proton events on long time scales. *Journal of Geophysical Research*, 113, D02302. <https://doi.org/10.1029/2007JD008574>
- Yando, K., Millan, R. M., Green, J. C., & Evans, D. S. (2011). A Monte Carlo simulation of the NOAA POES Medium Energy Proton and Electron Detector instrument. *Journal of Geophysical Research*, 116, A10231. <https://doi.org/10.1029/2011JA016671>
- Yokoyama, N., & Kamide, Y. (1997). Statistical nature of geomagnetic storms. *Journal of Geophysical Research*, 102(A7), 14,215–14,222. <https://doi.org/10.1029/97JA00903>
- Yonker, J. D. (2013). Contribution of the first electronically excited state of molecular nitrogen to thermospheric nitric oxide, (Ph.D. thesis). Zawecke, A. E., Tyssøy, H. N., Hibbins, R., Espy, P. J., Ødegaard, L.-K. G., Sandanger, M. I., & Stadsnes, J. (2016). The impact of energetic electron precipitation on mesospheric hydroxyl during a year of solar minimum. *Journal of Geophysical Research: Space Physics*, 121, 5914–5929. <https://doi.org/10.1002/2016JA022371>